Rapid Communications Editors' Suggestion

$BiMnTeO_6$: A multiaxis Ising antiferromagnet

N. Matsubara,[1,2] S. Petit,[2] C. Martin,[1] F. Fauth,[3] E. Suard,[4] S. Rols,[4] and F. Damay[2,*]

[1]*CRISMAT, 6 Bvd. Maréchal Juin, 14050 Caen Cedex, France*
[2]*Laboratoire Léon Brillouin, CEA-CNRS UMR12, Université Paris-Saclay, 91191 Gif sur Yvette Cedex, France*
[3]*CELLS ALBA Synchrotron, E-08290 Barcelona, Spain*
[4]*Institut Laue-Langevin, 71 Avenue des Martyrs, 38042 Grenoble Cedex 9, France*

(Received 27 July 2019; revised manuscript received 9 November 2019; published 12 December 2019)

The crystal and magnetic properties of honeycomb $BiMnTeO_6$ have been studied between 1.5 and 300 K using synchrotron x-rays and neutron-scattering experiments. Commensurate magnetic ordering is observed below $T_N = 10$ K, and corresponds to a noncollinear spin arrangement, with spins tilted away from the anisotropy easy-axis set by the Jahn-Teller distortion of the MnO_6 octahedra. Inelastic-scattering experiments show two main nearly localized magnetic excitations, which can be well described by an exchange Hamiltonian involving weak Mn-Mn magnetic interactions and a crystal-field Hamiltonian characterizing the strong easy-axis anisotropy associated with the d_{z2} orbital ordering of Mn^{3+}. The crystal-field levels can be accurately calculated, taking into account a transverse molecular field imposed by the magnetic ordering of the neighboring atoms below T_N. This makes $BiMnTeO_6$ an interesting example of a multiaxis Ising system in a self-imposed transverse magnetic field.

DOI: 10.1103/PhysRevB.100.220406

I. INTRODUCTION

In the transverse Ising magnet, a magnetic field applied transverse to the spin easy-axis induces a zero Kelvin phase transition from the magnetically ordered state to a disordered, yet correlated, state [1–4]. The transverse field Ising magnet (TFIM) is now the archetypal example of a system displaying a quantum phase transition [5]. Its widespread use relies on the fact that the application of a transverse field is a simple—and controllable—way to introduce quantum dynamics in an otherwise classical (Ising) system [6,7]. It is a customary tool in many relevant topics like quantum magnetism [8,9], or novel topological excitations [10], but also for understanding materials with unconventional properties, such as heavy fermion systems [11] and high-temperature superconductors [12]. It has been shown to successfully address anisotropic quantum phase transitions in spin chains, such as, for instance, $LiHoF_4$ [13,14], $BaCo_2V_2O$ [15], or the quantum critical point of $CoNb_2O_6$ [9,16], while being also at the heart of more subtle phenomena governing the stability of the quantum spin ice phase in some pyrochlore materials [17–21], or of the intertwined polar and multipolar order on the triangular lattice magnet $TmMgGaO_4$ [22].

In this Rapid Communication, we show that the low-energy properties of the layered honeycomb tellurate $BiMnTeO_6$ fall into TFIM physics [23]. X-ray and neutron diffraction demonstrate that this material hosts a zigzaglike pattern of orbital orientations, resulting in Mn^{3+} site-dependent magnetic easy axes. Below $T_N = 10$ K, those anisotropies compete with exchange interactions, to stabilize a noncollinear magnetic order, out of which emerges a specific spectrum of nearly localized magnetic excitations, as observed by inelastic neutron scattering. This spectrum can be correctly modeled by considering spins with large easy-axis magnetic anisotropy, yet coupled by a molecular field arising from the ordering of neighboring Mn^{3+} spins. This molecular field is characterized by a sizable component transverse to the local easy-axis directions.

II. EXPERIMENT

A. Synthesis

$BiMnTeO_6$ was prepared by conventional solid-state reaction, starting from a mixture of Bi_2O_3, Mn_2O_3, and H_6TeO_6. Stoichiometric amounts of precursors were mixed in an agate mortar, before being calcined in alumina crucibles at 700 °C for 24 h in O_2 flow. The powder was then ground, pressed into bars (~2 × 2 × 12 mm) with a uniaxial press, and sintered at 750 °C for 12 h in O_2 flow.

The obtained dark-brown powder of $BiMnTeO_6$ was then characterized by laboratory x-ray powder diffraction on a D8 ADVANCE Vario1 (Bruker) diffractometer (Cu$-K\alpha_1$ radiation); the monoclinic cell parameters [space group: $P2_1/c$, $a = 5.173(1)$ Å, $b = 9.058(1)$ Å, $c = 9.914(1)$ Å, $\beta = 90.17(1)°$] used to index the diffraction pattern were found to be in excellent agreement with [23].

B. Synchrotron x-ray and neutron diffraction

Synchrotron x-ray powder diffraction (SXRPD) experiments were performed on BL04-MSPD (ALBA), at RT and 6 K with the wavelength $\lambda = 0.442746$ and 0.442942 Å, respectively, using a rotating glass (Ø 0.3 mm) capillary tube and the position-sensitive detector MYTHEN. Neutron powder diffraction (NPD) was performed on the D2B (ILL, Grenoble; $\lambda = 1.595$ Å) and G4.1 diffractometers (CEA-Saclay, France; $\lambda = 2.426$ Å), at RT and from 1.5 to 300 K, respectively.

*Corresponding author: francoise.damay@cea.fr

 ©2019 American Physical Society

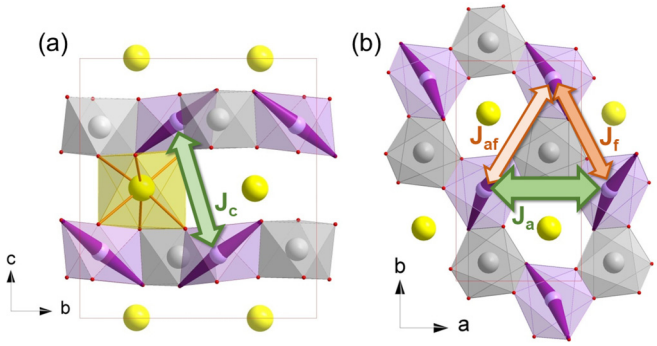

FIG. 1. $BiMnTeO_6$ structure viewed along a (a) and in the ab plane (b), showing corrugated planes separated by Bi cations, the Mn/Te order, and the d_{z2} orbitals orientation (longest axis of the MnO_6 octahedra, shown as thick purple lines). Bi (Mn/Te/O) atoms are symbolized as yellow (purple/gray/red) spheres. Magnetic exchange paths J_C, J_{af}, J_f, and J_a are also shown (see text).

Symmetry analysis and Rietveld refinements were performed with tools from the FULLPROF suite [24] and the Bilbao Crystallographic Server [25–28].

C. Inelastic neutron scattering

Time-of-flight (TOF) inelastic neutron-scattering experiments (INS) were performed using the thermal spectrometer IN4 (ILL, Grenoble), with two incident wavelength settings ($\lambda_i = 2.2$ and 3.4 Å), at 5 and 20 K. At 3.4 Å, the instrumental resolution is ∼0.5 meV. INS experiments were also performed on a triple-axis spectrometer at LLB-Orphée (4F2, $k_f = 1.55$ Å^{-1}). Higher-order contaminations were removed with a nitrogen-cooled Be filter placed in the scattered beam. The calculations presented in the study have been carried out with the code developed in Refs. [29,30].

III. RESULTS AND DISCUSSION

A. Crystal structure

The crystal structure of $BiMnTeO_6$ at RT has been refined in the monoclinic $P2_1/c$ space group (No. 14), starting from the unit cell and atomic coordinates reported by Kim *et al.* [23]. This structural model provides excellent fitting to both the SXRPD and NPD data (Supplemental Material Figs. S.1(a), S.1(b), and S.2 and Supplemental Material Tables S.I, S.II, and S.III [31]), and the corresponding structure is illustrated in Fig. 1. $BiMnTeO_6$ can be described accordingly as a distorted honeycomb structure, closely related to trigonal $BiFeTeO_6$ or $BiCrTeO_6$ [23,32]. This two-dimensional crystal structure is made of edge-sharing MnO_6 and TeO_6 octahedra forming honeycomb layers in the ab plane, with Bi^{3+} cations sandwiched between two such layers [Fig. 1(a)]. Importantly, the Mn and Te cations are fully ordered (within the refinement standard deviation), in contrast to Cr and Fe analogs [23]: the resulting topology of the Mn lattice is stacked distorted triangular planes [Fig. 1(b)]. The lower symmetry structure of $BiMnTeO_6$ (with respect to its trigonal parents) is caused by the Jahn-Teller (JT) distortion of $Mn^{3+}O_6$ octahedra, which are strongly elongated (Tables S.III and S.IV [31]). In $BiMnTeO_6$, the resulting orbital ordering pattern is a zigzag one, consisting of alternating rows with two different orbital orientations, as illustrated in Fig. 1(b).

The $P2_1/c$ structural model also fits the synchrotron data at 6 K (Tables S.I–S.III [31]), showing the absence of a structural phase transition going across the magnetic ordering transition at T_N. Close inspection of the data of Table S.II [31] shows remarkably little structural change (less than 0.13%) between 300 and 6 K, indicating that the zigzag orbital pattern remains unchanged in that temperature range.

B. Magnetic structure

From the Curie-Weiss fitting of the paramagnetic range (see Fig. S.3 [31] and [23]), weak but clearly predominantly antiferromagnetic interactions are expected to govern the magnetic ordering of $BiMnTeO_6$. The evolution of the neutron diffraction patterns shows the appearance of new Bragg peaks below $T_N = 10$ K [Figs. 2(a) and 2(b)], corroborating long-range magnetic ordering. All the magnetic Bragg peaks can be indexed with a commensurate propagation vector $\mathbf{k} = (\frac{1}{2}\ 0\ 0)$. To constrain the number of solutions for the magnetic models, a symmetry analysis was carried out, for the Wyckoff site 4e of Mn. There are four irreducible representations of dimension 1, each containing three basis vectors: $\Gamma_m = 3\Gamma_1 \oplus 3\Gamma_2 \oplus 3\Gamma_3 \oplus 3\Gamma_4$. The best agreement with the experimental data is obtained for the Γ_1 representation, whose basis vectors are given in Table S.V [31]. For the single independent magnetic atom of the asymmetric unit cell, the three magnetic components m_x, m_y, and m_z can be refined independently. At 1.5 K, the Rietveld refinement [Fig. 2(c)] yields $m_x = 1.7(1)$, $m_y = -1.6(1)$, and $m_z = 2.8(1)$, which gives an ordered magnetic moment value of of $3.7(2)\mu_B$, close to the expected value of $4\mu_B$ for Mn^{3+} ($S = 2$). The resulting noncollinear magnetic structure is illustrated in Fig. 2(d). Its main features are antiferromagnetic chains of parallel spins running along a, the spin direction in two adjacent chains approximately following the zigzag orbital pattern described earlier, with an ∼20° canting angle with respect to the local longest axis. This magnetic structure corresponds to the Shubnikov group P_a2_1/c (No. BNS 14.80), whose magnetic point group $2/m1'$ leads to zero polarization and magnetoelectric tensors.

C. Magnetic excitations

Figure 3 shows the inelastic powder spectra of $BiMnTeO_6$ mapped over momentum and energy transfer at 5 and 20 K. Remarkably, the dominant feature of the spectrum at 5 K is a strong almost flat band around 2 meV [Figs. 3(a) and 3(c)], whose intensity decreases with increasing Q as expected for magnetic scattering. This mode seems to slightly soften and broaden for $0.6 < Q < 0.9$ Å^{-1}, indicating a very weak dispersion. There is no dispersive magnetic signal originating from the magnetic Bragg positions around $Q = 0.6$ and 0.9 Å^{-1}, however [Fig. 3(c)]. Another weaker flat band is also observed around 3 meV. The evolution with temperature of constant $Q = 0.8$ Å^{-1} cuts is illustrated in Fig. 3(d) and shows clearly the existence, as high as 50 K (i.e., far above T_N), of a magnetic signal (peaking around 1.5 meV), which evolves continuously across the magnetic transition to split into two levels at 2 and 3 meV. This behavior strongly suggests that

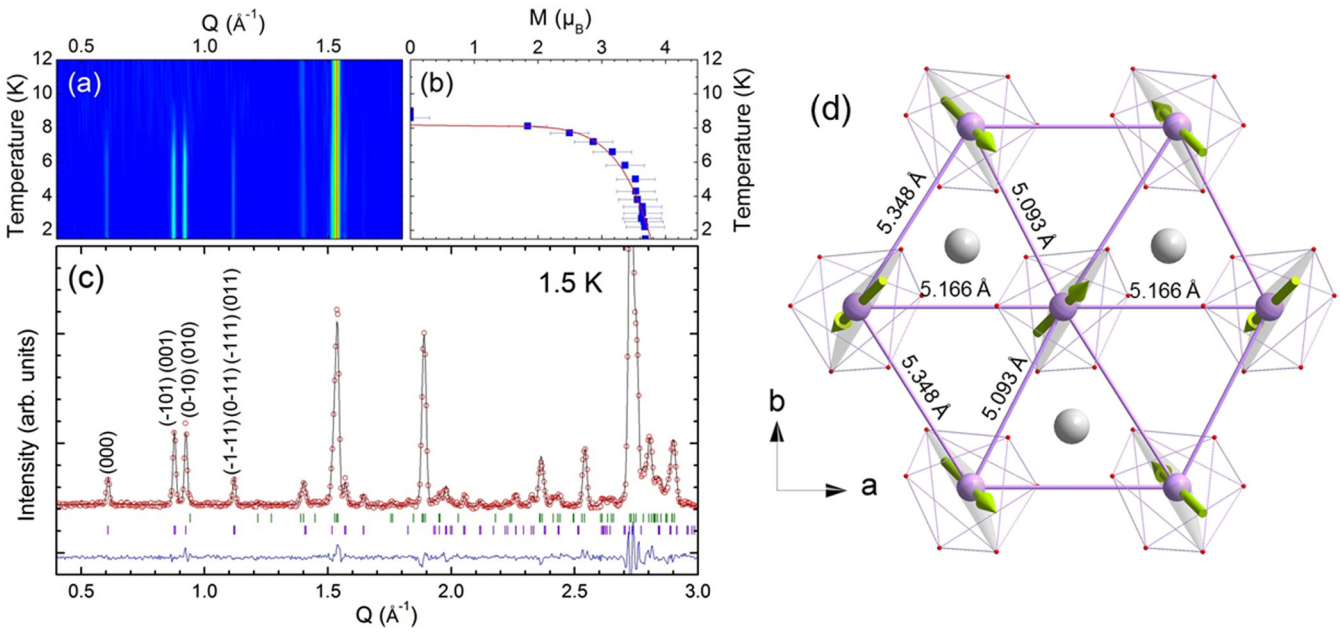

FIG. 2. (a) Temperature evolution of the NPD data (G4.1) between 1.5 and 12 K. (b) Corresponding temperature evolution of the Mn ordered magnetic moment (from Rietveld refinement results). The red line is a guide to the eye. (c) Rietveld refinement of the NPD pattern at 1.5 K ($R_{\text{Bragg mag}} = 7.5\%$ and global $\chi^2 = 3.6$) (Experimental data: red open circles; calculated profile: black line; allowed Bragg reflections: vertical green marks; purple marks indicate magnetic Bragg reflections. The difference between the experimental and calculated profiles is displayed as a blue line.) (d) Magnetic structure of BiMnTeO$_6$ (Mn^{3+} spins are shown as green arrows, longest Mn-O bonds as thick gray shapes). First-neighbor Mn-Mn distances in the triangular lattices are indicated.

the magnetic spectrum is not composed of classical dispersing spin waves, but, rather, of magnetic excitons, corresponding primarily to crystal-field-like levels, which are modified by an internal molecular magnetic field as spins order below T_N and thus acquire a weak dispersion. This scenario can be modeled using the following Hamiltonian:

$$\mathcal{H} = \mathcal{H}_{\text{exch}} + \mathcal{H}_{\text{CEF}}. \tag{1}$$

Here

$$\mathcal{H}_{\text{exch}} = \sum_{i,j} J_{ij} \mathbf{J}_i \mathbf{J}_j$$

describes the exchange interactions between spins $\mathbf{J}_i$ and $\mathbf{J}_j$ at sites i and j, with J_{ij} the exchange coupling, and

$$\mathcal{H}_{\text{CEF}} = \sum_i \left[\sum_{l,m} B_{lm} O_{i,lm} \right]$$

describes the crystal-electric-field (CEF) -like Hamiltonian and characterizes the anisotropy of the $3d$ electron cloud around Mn^{3+}. From a general point of view, it is written in terms of the O_{nm} Stevens operators [33–35], while B_{lm} are the crystal-field coefficients.

In the specific case of BiMnTeO$_6$, all J_{ij} exchanges are considered first neighbor. They correspond to three interactions within the triangular plane, J_a, J_f, J_{af}, and to an interplane coupling J_C (Fig. 1). Mn^{3+} ions are located on the $4e$ site of the $P2_1/c$ structure, whose local symmetry is C_1. To avoid excessive overparametrization, only a single B_{20} term was taken into account in the CEF Hamiltonian. Such a choice can be argued to be rather crude; considering the low symmetry of the Mn^{3+} site, it is solidly warranted, however, by other examples of Mn^{3+} complexes with strong JT distortion, in which the axial parameter is at least ten times the rhombic one [36,37]. This B_{20} term corresponds to an easy-axis anisotropy ($B_{20} < 0$), as anticipated for Mn^{3+} in a JT distorted environment. Note that the main CEF z axis is set to *locally* correspond to the longest axis of the MnO$_6$ octahedron and thus changes from site to site according to the orbital pattern.

To determine the parameters of the model, the following procedure was applied. A first estimation of B_{20} was assessed from the position of the broad energy level observed at 20 K (i.e., when $H_{\text{exch}} = 0$, above T_N), at ~1.5 meV. This corresponds to $B_{20} = -0.17$ meV, in agreement with the expected axial magnetic anisotropy (see also Fig. S.4 [31]). We then solved Eq. (1) at the mean-field level for each site within the magnetic unit cell:

$$\begin{aligned}\mathcal{H}_{\text{MF}} &= \sum_{l,m} B_{lm} O_{i,lm} + \mathbf{J}_i \cdot \mathbf{H}_{\text{loc}} \\ &= \sum_{l,m} B_{lm} O_{i,lm} + \mathbf{J}_i \cdot \sum_j J_{ij} \langle \mathbf{J}_j \rangle.\end{aligned}$$

H_{loc} defines the molecular field experienced by a spin at site i. From analytical results, it is quickly inferred that the relevant parameters are $(J_a + J_C)$ and $(|J_f| + J_{af})$. A series of calculations was then performed, varying $(J_a + J_C)$ and $(|J_f| + J_{af})$. For each trial, the ground state ordered magnetic structure was determined by such self-consistent calculations. The excitonic spectrum was computed subsequently in the random phase approximation, along with the corresponding inelastic neutron cross section.

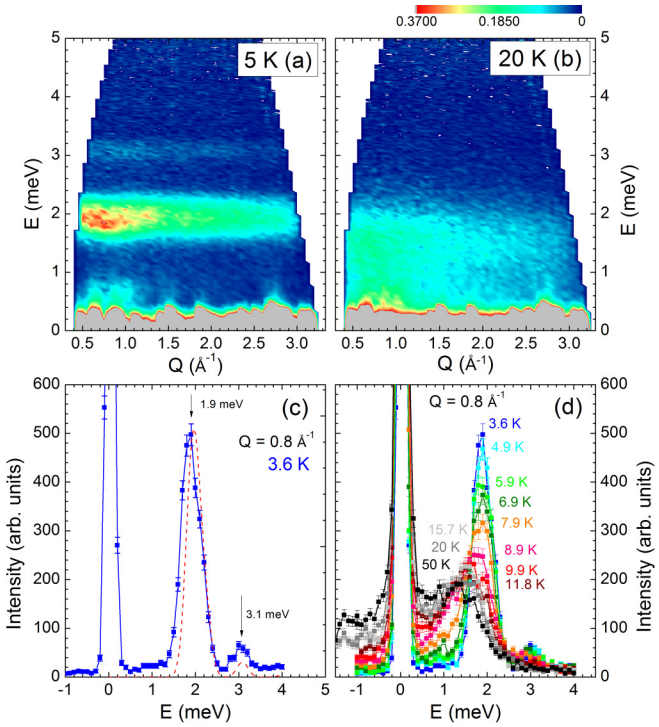

FIG. 3. TOF INS data (IN4) of $BiMnTeO_6$ at 5 K (a) and 20 K (b) (incident wavelength 3.2 Å). No additional excitation, whether of magnetic or lattice origin, are seen up to 15 meV. (c) Constant $Q = 0.8$ Å^{-1} cut (4F2) at 3.6 K, showing the two modes at 1.8 and 3.1 meV. The dotted red line is calculated using Hamiltonian (1) with parameters $B_{20} = -0.17$ meV, $(J_a + J_C) = 0.14$ meV, $(J_{af} + |J_f|) = 0.08$ meV. (d) Temperature evolution (up to 50 K) of constant $Q = 0.8$ Å^{-1} cuts.

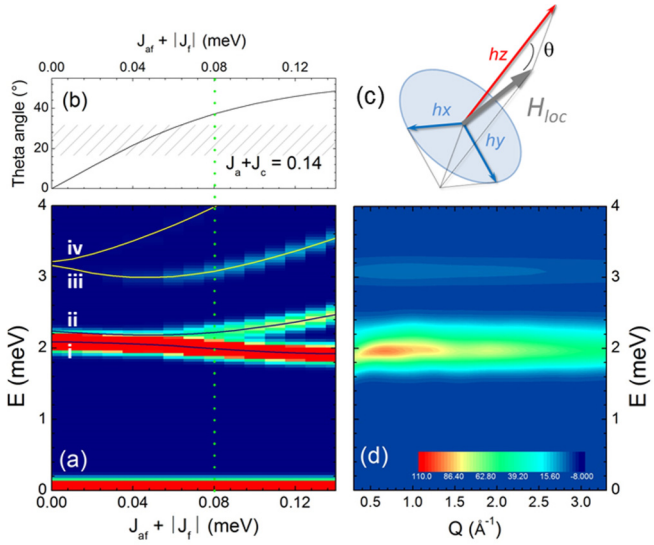

FIG. 4. (a) Calculated variation with $(J_{af} + |J_f|)$ of the neutron cross section of Mn^{3+} crystal-field transitions $[(J_a + J_C) = 0.14$ meV, $B_{20} = -0.17$ meV$]$. (b) Corresponding variation with $(J_{af} + |J_f|)$ of the angle between the anisotropy axis (axis of longest elongation of the MnO_6 octahedron, set parallel to hz) and the internal magnetic field H_{loc}. In (a) and (b) the green dotted line corresponds to the set of parameters giving the best agreement with the experimental data. (c) Schematic drawing of H_{loc} and of its projection hx and hy (transverse components) and hz (longitudinal component). If $hx = hy = 0$, and $hz \neq 0$, the molecular field is purely longitudinal. (d) Calculations of the powder average INS excitation spectrum of $BiMnTeO_6$ (at 0 K), based on Hamiltonian (1), with parameters $B_{20} = -0.17$ meV, $(J_a + J_C) = 0.14$ meV, $(J_{af} + |J_f|) = 0.08$ meV [calculations include the Mn magnetic form factor for direct comparison with Fig. 3(a)].

Calculations show that if $(|J_f| + J_{af}) = 0$, increasing $(J_a + J_C)$ leads to a linear increase of the energy position of the four Mn^{3+} crystal-field levels, with only one mode being neutron active (Fig. S.4 [31]). For instance, for $(|J_f| + J_{af}) = 0$ and $(J_a + J_C) = 0.14$ meV, four energy levels are calculated, at 2.09 meV (i), 2.24 meV (ii), 3.16 meV (iii), and 3.21 meV (iv), with only (i) having a nonzero neutron cross section [Fig. 4(a)]. In this $(|J_f| + J_{af}) = 0$ case, the molecular field at a given site is purely longitudinal (i.e., along the local z axis) and proportional to $(J_a + J_C)$.

A more complex picture emerges when $(|J_f| + J_{af}) \neq 0$. With increasing $(|J_f| + J_{af})$, a progressive increase of the calculated intensities of the (ii) and (iii) levels is observed, so that they become visible for $(|J_f| + J_{af}) > 0.06$ meV [Fig. 4(a)]. Further increasing $(|J_f| + J_{af})$ leads eventually to a clear splitting of the calculated (i) and (ii) levels above $(|J_f| + J_{af}) \sim 0.09$ meV, as the energy position of the (i) level decreases, while that of the (ii) level increases. When $(|J_f| + J_{af})$ is $\neq 0$, the molecular field is not purely longitudinal anymore, as increasing $(|J_f| + J_{af})$ is equivalent to increasing the transverse components of the molecular field [Figs. 4(b) and 4(c)].

Using Fig. 4(a), a good modeling of the experimental data is obtained for $(|J_f| + J_{af}) = 0.08$ meV [with $B_{20} = -0.17$ meV and $(J_a + J_C) = 0.14$ meV]. The corresponding calculated powder averaged excitation spectrum, convoluted with the Mn^{3+} magnetic form factor, is shown in Fig. 4(d), and gives excellent agreement with the experimental results of Fig. 3(a). A comparison between experimental and calculated $Q = 0.8$ Å^{-1} profiles is also given in Fig. 3(c), to illustrate the very good match between the observed and computed positions, and relative intensities, of the two modes. The slight dispersion of the 2 meV exciton level is also reproduced by the calculation, although it is somewhat blurred in Fig. 4(d), because of the powder average and the resolution function that is used to match experimental data. In the ordered spin configuration calculated as the ground state for this set of parameters, spins are tilted by 37° from their local anisotropy axis, which lies slightly above the range expected from diffraction results [Fig. 4(b)].

IV. DISCUSSION

The microscopic magnetic properties of electrons in transition metal and rare-earth magnetic compounds are determined mainly by exchange and crystal-field effects and their relative magnitudes. In conventional transition metal compounds, isotropic magnetic exchanges being dominant, the elementary excitations are spin waves, which are dispersive by nature. Crystal-field effects appear only as small correction terms, contributing to the magnetic anisotropy. In systems with

weak magnetic exchanges and consequently low ordering temperatures (typically below 10 K), crystal-field effects are now expected to predominate: excitations correspond to local transitions between energy levels, and characterize the ground state electronic structure. Typical examples of the latter case are $4f$ compounds [35]. With regard to transition metals, most studies are performed on metal complexes with very weak magnetic interactions, such as molecular magnets or clusters [37], to better apprehend magnetic anisotropies or intracluster exchanges, and high-spin to low-spin transitions. $LaCoO_3$ in its $S = 0$ state is a rare example of a transition metal oxide in which neutron spectroscopic techniques have investigated the CEF energy levels [38].

$BiMnTeO_6$ is therefore a rather unusual example of a transition metal oxide, in which noncollinear magnetic ordering is set by the strong easy-axis anisotropy imposed by the orbital ordering and in which magnetic exchange arises as a perturbation, quantified through the temperature evolution of the crystal-field excitations at T_N.

An important outcome of this study is that it is the transverse components of the local magnetic field which are responsible for the splitting of the crystal-field levels. $BiMnTeO_6$ can be therefore described as a full member of the TFIM family, whose originality resides in the zigzag orbital pattern imposing noncollinear easy-axis anisotropies. The strong potential of the honeycomb tellurates $AMTeO_6$ as a tunable TFIM system relies in the possibility to adjust long-range exchange interactions and easy-axis anisotropy character depending on the size and nature of the A and M cations. Other means, such as applied external magnetic field or pressure, could also be used to modify the ratio between the local transverse magnetic field and the easy-axis magnetic anisotropy, to determine, for instance, the threshold value of the transverse field at which a quantum phase transition is observed.

V. CONCLUSION

An experimental realization of the transverse field Ising model has been evidenced in $BiMnTeO_6$. Magnetic ordering sets in at $T_N = 10$ K, the magnetic ground state being made of noncollinear magnetic spins, which follow the zigzag pattern of d_{z2} orbitals existing at RT, but deviating by $\sim 20^\circ$ from their local anisotropy axis. Above T_N, the existence of a broad mode peaking at 1.5 meV is attributed to a crystal-field exciton. Below T_N, this mode splits into two separate barely dispersive modes at ~ 2 and ~ 3 meV, of very distinct intensities. By means of self-consistent calculations based on a conventional Hamiltonian, using three independent parameters only, $B_{20} = -0.17$ meV, $(J_a + J_C) = 0.14$ meV, and $(|J_f| + J_{af}) = 0.08$ meV, all these experimental observations can be well reproduced. Calculations also show that the temperature dependence of the crystal-field excitations originates from the increasing transverse component of the molecular field, which arises as Mn^{3+} spins order.

ACKNOWLEDGMENT

This work was partially supported by the IUCr2017-STOE grant, awarded to N.M.

[1] R. J. Elliott, P. Pfeuty, and C. Wood, Phys. Rev. Lett. **25**, 443 (1970).
[2] P. Pfeuty, Ann. Phys. (NY) **57**, 79 (1970).
[3] P. Pfeuty and R. J. Elliott, J. Phys. C: Solid State Phys. **4**, 2370 (1971).
[4] *Quantum Ising Phases and Transitions in Transverse Ising Models*, edited by B. K. Chakrabarti, A. Dutta, and P. Sen (Springer, Berlin, 1996).
[5] S. Sachdev, *Quantum Phase Transitions* (Cambridge University Press, Cambridge, UK, 1999).
[6] C.-J. Lin, C.-N. Liao, and C.-H. Chern, Phys. Rev. B **85**, 134434 (2012).
[7] P. Emonts and S. Wessel, Phys. Rev. B **98**, 174433 (2018).
[8] S. Ghosh, T. F. Rosenbaum, G. Aeppli, and S. N. Coppersmith, Nature (London) **425**, 48 (2003).
[9] R. Coldea, D. A. Tennant, E. M. Wheeler, E. Wawrzynska, D. Prabhakaran, M. Telling, K. Habicht, P. Smeibidl, and K. Kiefer, Science **327**, 177 (2010).
[10] J. Alicea, Rep. Prog. Phys. **75**, 076501 (2012).
[11] Q. M. Si and F. Steglich, Science **329**, 1161 (2010).
[12] S. Sachdev, Phys. Status Solidi B **247**, 537 (2010).
[13] D. Bitko, T. F. Rosenbaum, and G. Aeppli, Phys. Rev. Lett. **77**, 940 (1996).
[14] H. M. Ronnow, R. Parthasarathy, J. Jensen, G. Aeppli, T. F. Rosenbaum, and D. F. McMorrow, Science **308**, 389 (2005).
[15] Q. Faure, S. Takayoshi, S. Petit, V. Simonet, S. Raymond, L.-P. Regnault, M. Boehm, J. S. White, M. Mansson, C. Rueegg, P. Lejay, B. Canals, T. Lorenz, S. C. Furuya, T. Giamarchi, and B. Grenier, Nat. Phys. **14**, 716 (2018).
[16] T. Liang, S. M. Koohpayeh, J. W. Krizan, T. M. McQueen, R. J. Cava, and N. P. Ong, Nat. Commun. **6**, 7611 (2015).
[17] J. Villain, R. Bidaux, J. P. Carton, and R. Conte, J. Phys. **41**, 1263 (1980).
[18] R. Moessner, S. L. Sondhi, and P. Chandra, Phys. Rev. Lett. **84**, 4457 (2000).
[19] L. Savary and L. Balents, Phys. Rev. Lett. **118**, 087203 (2017).
[20] N. Martin, P. Bonville, E. Lhotel, S. Guitteny, A. Wildes, C. Decorse, M. Ciomaga Hatnean, G. Balakrishnan, I. Mirebeau, and S. Petit, Phys. Rev. X **7**, 041028 (2017).
[21] O. Benton, Phys. Rev. Lett. **121**, 037203 (2018).
[22] Y. Shen, C. Liu, Y. Qin, S. Shen, Y.-D. Li, R. Bewley, A. Schneidewind, G. Chen, and J. Zhao, Nat. Commun. **10**, 4530 (2019).
[23] S. W. Kim, Z. Deng, Z. Fischer, S. H. Lapidus, P. W. Stephens, M. R. Li, and M. Greenblatt, Inorg. Chem. **55**, 10229 (2016).
[24] J. Rodriguez-Carvajal, Phys. B **192**, 55 (1993).
[25] M. I. Aroyo, A. Kirov, C. Capillas, J. M. Perez-Mato, and H. Wondratschek, Acta Crystallogr., Sect. A **62**, 115 (2006).

[26] E. Kroumova, M. I. Aroyo, J. M. Perez-Mato, A. Kirov, C. Capillas, S. Ivantchev, and H. Wondratschek, Phase Transitions **76**, 155 (2003).
[27] J. M. Perez-Mato, D. Orobengoa, and M. I. Aroyo, Acta Crystallogr., Sect. A **66**, 558 (2010).
[28] D. Orobengoa, C. Capillas, M. I. Aroyo, and J. M. Perez-Mato, J. Appl. Crystallogr. **42**, 820 (2009).
[29] S. Petit, Collection SFN **12**, 105 (2011).
[30] S. Petit, E. Lhotel, B. Canals, M. C. Hatnean, J. Ollivier, H. Mutka, E. Ressouche, A. R. Wildes, M. R. Lees, and G. Balakrishnan, Nat. Phys. **12**, 746 (2016).
[31] See Supplemental Material at http://link.aps.org/supplemental/10.1103/PhysRevB.100.220406 for additional diffraction and magnetisation data; Complementary modelling calculations; and Tables with Rietveld refinement and symmetry analysis results.
[32] B. G. Vats, R. Phatak, K. Krishnan, and S. Kannan, Mater. Res. Bull. **48**, 3117 (2013).
[33] M. T. Hutchings, Solid State Phys. **16**, 227 (1964).
[34] A. Mackintosh and H. Moller, *Magnetic Properties of Rare-Earth Metals* (Plenum, New York, 1972).
[35] B. G. Wybourne, *Spectroscopic Properties of Rare Earth* (Wiley, New York, 1965).
[36] K. Ridier, S. Petit, B. Gillon, G. Chaboussant, D. A. Safin, and Y. Garcia, Phys. Rev. B **90**, 104407 (2014).
[37] R. Basler, P. L. W. Tregenna-Piggott, H. Andres, C. Dobe, H. U. Gudel, S. Janssen, and G. J. McIntyre, J. Am. Chem. Soc. **123**, 3377 (2001).
[38] A. Podlesnyak, S. Streule, J. Mesot, M. Medarde, E. Pomjakushina, K. Conder, A. Tanaka, M. W. Haverkort, and D. I. Khomskii, Phys. Rev. Lett. **97**, 247208 (2006).